The Size-Dependent Ferroelectric Phase Transition in BaTiO₃ Nanocrystals Probed by Surface Plasmons

Daniel Szwarcman, Daniel Vestler, and Gil Markovich*

School of Chemistry, Raymond and Beverly Sackler Faculty of Exact Sciences, Tel-Aviv University, Tel-Aviv, 69978, Israel

ABSTRACT A new technique for probing the temperature dependence of the dielectric constant of ferroelectric nanocrystals (NCs) using shifts in the localized surface plasmon resonance (LSPR) wavelength of gold nanoparticles attached to the surface of the ferroelectric NCs is demonstrated. This technique can selectively probe the surface of the NCs and was used to study the ferroelectric-to-paraelectric phase transition of barium titanate (BTO) nanocubes in three size regimes of 16 ± 4, 47 ± 11, and 220 ± 140 nm. Temperature-dependent Raman spectroscopy was also applied to probe the whole volume of the NCs. The LSPR-based technique revealed that the ~16 nm BTO NCs were dominated by surface effects, and as the NC size increased bulk BTO behavior governed. This supports recent propositions about the lack of intrinsic size dependence of the transition temperature. Therefore, the surface chemistry/structure probably affected the ferroelectric behavior rather than finite size effects. A distinct phase transition at the surface characterized by a very long relaxation time was detected by the LSPR-based technique.

KEYWORDS: barium titanate nanocrystals · ferroelectric size effects · thermal hysteresis · surface effects · local surface plasmon resonance

Understanding the fundamental aspects of nanoscale ferroelectricity is important for various applications of ferroelectric materials, such as non-volatile memories and pyroelectric and piezoelectric devices.[1−6] Ferroelectricity is a cooperative phenomenon of interacting dipoles stemming mainly from ionic polarization, that is, the relative displacement of the positive and negative sublattices in an ionic crystal. For example, in the perovskite prototype material BaTiO₃ (BTO), ferroelectricity arises due to a displacement of Ti atoms from their centrosymmetric position in the unit cell. At the nanoscale, and in particular at NCs that are strongly confined in three-dimensions the regular domain structure becomes energetically unfavorable due to the energy penalty for forming domain walls. On the other side, since single domain structures would also be unstable due to large depolarization fields, deviations from "bulk" properties are expected. This leads to the idea of a critical correlation volume below which ferrolelectricity cannot be sustained.[7] Some theoretical[8−11] and experimental[12] reports address the size-dependent phase transition properties but only few concentrate specifically on individual NCs. While several studies of perovskite nanoparticles,[13] thin films,[14] and multidomain ferroelectric lamellae cut by focused ion beams down to ~70 nm[15] indicate a bulk-like phase transition behavior, other reports on nanopowders,[16−18] grained ceramics,[19] nanowires,[20] and thin films[2,3,5,21] indicate a drop in Curie temperature (T_C) with decreasing grain size or film thickness. However, for individual well-separated NCs the critical volume has not been conclusively established. Values reported for BTO estimate a critical size of the order of 10 nm while others estimate only a few unit cells for thin films[11,21−23] that may possibly exhibit novel geometric ordering.[24] Studies on grained BTO ceramics even argue that no size limit exists but rather the ferroelectricity weakens exponentially with size.[25] Discrepancies in the size-dependent phase transition temperature may arise from extrinsic effects, for example, composition,[26] defects,[19] strain,[27] and surface charging.[28] Some investigations indicate that nanoscale ferroelectrics exhibit a smeared or diffuse phase-transition still having bulk-like T_C;[13] however, this has been explained as a pure surface effect, related to local compositional surface potential inhomogeneity at the surface.[29,30]

Early studies by Tanaka on powder X-ray diffraction data (XRD) of BTO NCs[16] and later studies by Hoshina *et al.*[31] and others suggested that the surface of such NCs is always relaxed to the cubic paraelectric phase while the core is in the tetragonal ferroelectric phase and that at small enough NCs the surface effect dominates and the

nanocrystals lose their ferroelectricity. Raman scattering was also used to study structural transitions in ferroelectric materials and determine T_C in ferroelectric bulk, thin films, and nanoparticles.[32]

Volume-averaging structural characterization techniques such as XRD and Raman scattering are insensitive to NC surface effects. In particular, as NC size decreases and the surface layer takes a substantial part of the volume an average over surface and interior would be measured using these techniques.[11,29,33,34] Scanning probe microscopy based methods are widely used to examine ferroelectric surfaces and provide valuable information on surface potential and local electromechanical properties with high lateral resolution.[6,7,35−40] Noncontact techniques such as scanning surface potential microscopy and electric force microscopy are sensitive to surface charges, which for ferroelectric surfaces originate in a mixture of fast dipolar polarization and slower mobile charges which may be partially resolved by analyzing temporal behavior.[41] To resolve the fundamental questions regarding nanoscale ferroelectricity and the nature of the ferroelectric phase transition on going to the nanoscale, a technique which would be selectively sensitive to the ferroelectric polarization behavior at the surface of the ferroelectric NCs, without interference of mobile charges, is required. Such a technique, utilizing gold nanoparticles (GNPs) as plasmonic probes of surface ferroelectric transitions in BTO NCs is presented in this paper.

GNPs exhibit a strong visible extinction band due to their LSPR.[42−45] LSPR excitation results in enhanced local electromagnetic fields near the surface of the GNPs. The peak wavelength, λ_{max}, of the LSPR spectrum is dependent not only on the size, shape, and free electron density of the GNPs but also on their local environment high frequency dielectric properties (e.g., refractive index).[46−49] Plasmonic metal nanoparticles have attracted great attention due to their potential application in chemical[50] and biochemical[51,52] sensing and enhancement of various optical effects.[43,53] The sensitivity of λ_{max} to the dielectric environment strongly decays as a function of distance away from the surface of the GNPs, with a decay length of the order of a few nanometers. Accordingly, a plasmonic sensor, such as a GNP, is sensitive to dielectric changes only adjacent to its surface.

Consequently, in the present work we demonstrate an indirect method capable of selectively probing near-surface dielectric changes of ferroelectric NCs using a LSPR sensing approach. Temperature-dependent LSPR absorption peaks of metal nanoparticles attached to ferroelectric NC surfaces were used to probe the ferroelectric to paraelectric phase transition of the BTO NCs. Since the probing is done at optical frequencies the technique is insensitive to relatively slow compensating charge motions but susceptible to tightly bound electron distribution changes due to nuclear distor-

tions. The phase transitions of BTO single crystal nanoparticles were studied for three size regimes: ca. 16 nm, 47 nm, and >0.1 μm, where the latter is commonly accepted as having ferroelectric bulk-like properties.[15]

The static dielectric constant of ferroelectric materials is known to sharply peak on passing through their T_C. The optical dielectric constant, $\varepsilon(\omega) = n^2$, where n is the refractive index, is also influenced by this transition in a similar manner, but with a more moderate change. In bulk BTO it is commonly accepted that there is an increase of ∼0.1 units of refractive index (RI) across the phase transition,[54,55] which should significantly shift the plasmon absorption peak of the GNPs attached to the BTO NCs toward longer wavelengths. Several studies estimate the dependence of the LSPR peak position of spherical GNPs in the wavelength range of 500−600 nm on the environment's refractive index to be about 70−200 nm per RI unit.[47,49] Similar results were obtained also in studies on the refractive index effect of the substrate on the LSPR of adsorbed gold and silver nanoparticles.[56,57] This leads to an expected GNP plasmon peak red-shift of the order of 10 nm due to the change in the RI of BTO with temperature going through T_C, considering also that the BTO fills only a fraction of the GNP surroundings.

RESULTS AND DISCUSSION

For the present study, surfactant-free BTO single crystal nanocubes were prepared by a molten hydroxide synthesis according to Liu et al.[58] The temperature of the synthesis was used to control the average NC size (see Methods section for synthesis details and Figure S1(a−f) in the Supporting Information showing TEM images of BTO NCs and their size distribution). Well-dispersed colloidal GNPs of about 10 nm in size were synthesized using a chemical reduction process. The GNPs were coated with charged bifunctional surfactant molecules containing both carboxylate and thiol groups, such as thioctic acid and mercaptopropionic acid that possess a strong affinity to the BTO surfaces, probably through electrostatic or hydrogen bonds between the carboxylates and the surface ions. Two types of samples were prepared: the smaller (∼16 nm and ∼47 nm BTO) BTO−Au hybrid particles could be studied as colloidal dispersions in polar solvents, such as tetraethylene glycol, while the larger bulk-like BTO−Au hybrids were deposited as a thin film on fused silica substrates. TEM images of the BTO−Au hybrid particles formed by mixing the aqueous dispersions of the GNPs and BTO NCs, with varying BTO NC size are shown in Figures 1a (16 ± 4 nm BTO), 3a (47 ± 11 nm BTO), and 4a (220 ± 140 nm BTO). While the aggregation in the BTO-GNP hybrids seen in the above-mentioned TEM images originates in the deposition of these hydrophilic BTO−Au hybrids on the carbon coated TEM grids from solution, the BTO−Au hybrids dispersed in liquid used
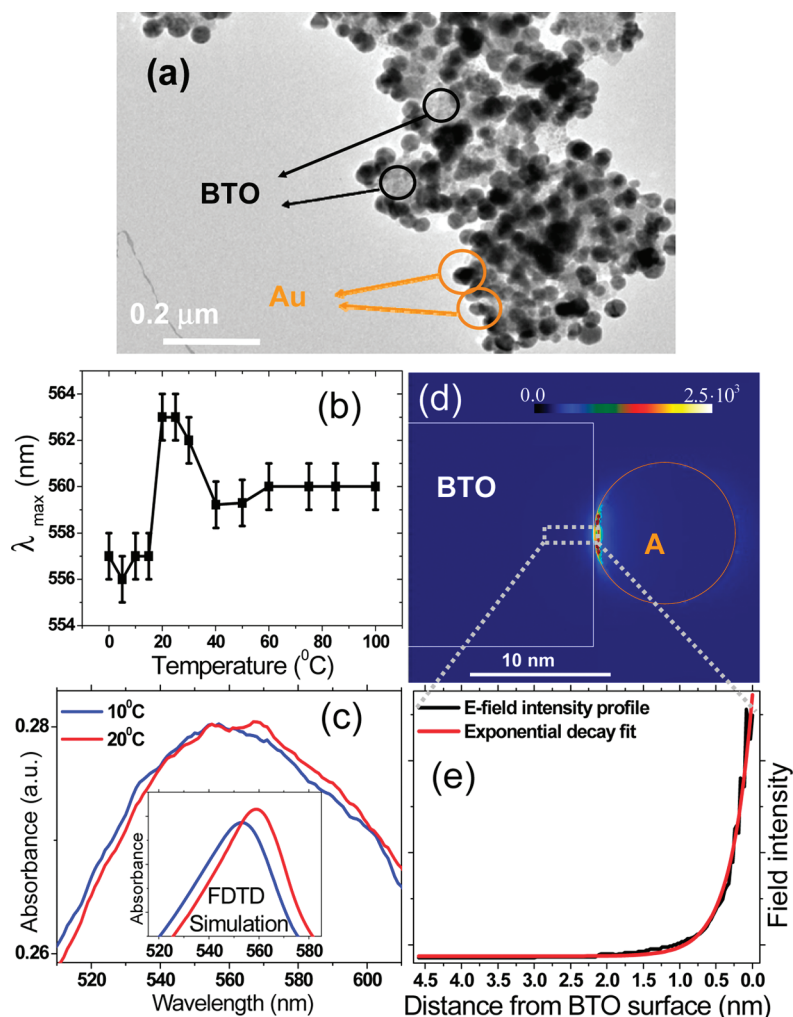
Figure 1. (a) TEM image of ~10 nm GNPs attached to the 16 nm BTO NCs. (b) Temperature-dependent plasmon peak wavelength of the GNPs shown in panel a. (c) Experimental plasmon peak at 10 and 20 °C of the GNPs attached to the 16 nm BTO NCs. Inset is the FDTD calculated optical response for a 10 nm gold nanoparticle attached to the facet of a ~20 nm BTO nanocrystal. A red-shift of ~6 nm in λ_{max} was observed. (d) The FDTD calculated average electric field intensity map for a GNP attached to a ~20 nm BTO NC. The color scale bar corresponds to the relative field enhancement factor. The plasmonic field decay profile from the GNP−BTO interface in to the BTO is shown in panel e. The RI values of BTO at room temperature and at bulk T_C were taken from ref 54.

in the experiments did not suffer from substantial aggregation and were stable over a period of 2 weeks.

The temperature dependence of the optical dielectric constant of the BTO NCs could be followed on a semiquantitative level by monitoring the shift in GNP LSPR peak wavelength, λ_{max}, as a function of temperature.

LSPR spectra were measured at several temperatures (raw data shown in Figure S2 in the Supporting Information). The LSPR spectra of the thin film samples were noisier due to the large scattering from the larger BTO NCs. Thus, a Gaussian fit to the LSPR peak in each spectrum was used to better estimate the peak location (see Supporting Information Figure S4). Figure 1b depicts the plasmon absorption peak position of ~10 nm GNPs attached to 16 ± 4 nm BTO NCs as a function of temperature, measured in a tetraethylene glycol dispersion. As the temperature reached ~25 °C, a sharp increase in the plasmon absorption peak wavelength, of

~7 nm, from ~557 to ~565 nm was seen, followed by a decrease to ~560 nm around 30 °C and remaining constant with further temperature increase. The blue-shift above 30 °C is probably due to increasing the temperature further above T_C where the optical dielectric constant is supposed to decrease. The dielectric constant usually peaks around T_C in ferroelectrics. Figure 1c demonstrates the experimental plasmon absorption peak wavelength shift between 10 °C−20 °C.

To verify that the magnitude of the LSPR red-shift on going through T_C conforms with the expected RI change we have performed finite difference time domain (FDTD) simulations of light extinction in a single 10 nm GNP attached to a 20 nm BTO NC. As seen in the inset of Figure 1c a λ_{max} shift of ~6 nm was obtained in the simulation when using an estimated bulk BTO refractive index change of about 0.15 RI units.[54,55] This calculated shift is similar to the shift observed in Figure 1b. The calculated electric field intensity map in
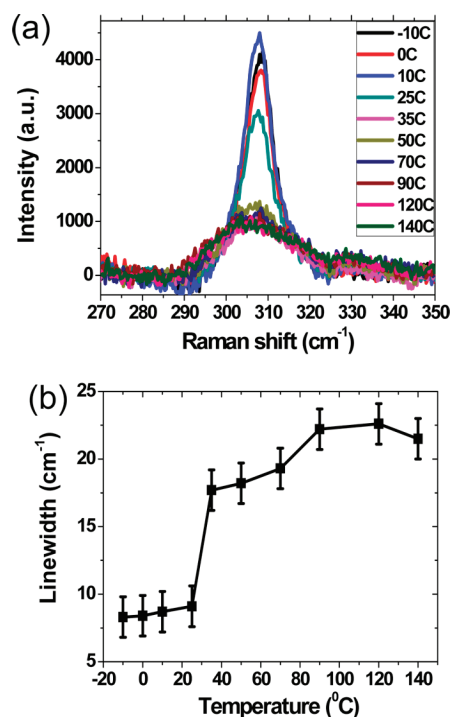
Figure 2. (a) Raman spectra around the 306 cm^{-1} band at different temperatures for the 16 nm BTO NCs. **(b)** Full width at half-maximum of the $\sim$306 cm^{-1} Raman peak as a function of temperature.

Figure 1d showed that the local electric field produced by the LSPR decays within $\sim$1 nm (see Figure 1e) into the BTO NC, and thus probed only the near surface layer of the BTO NCs.

Two control experiments of heating GNPs only and GNPs attached to SrTiO$_3$ (STO), a well-known paraelectric ternary oxide, within the temperature range used in the measurements, resulted in a negligible shift of the
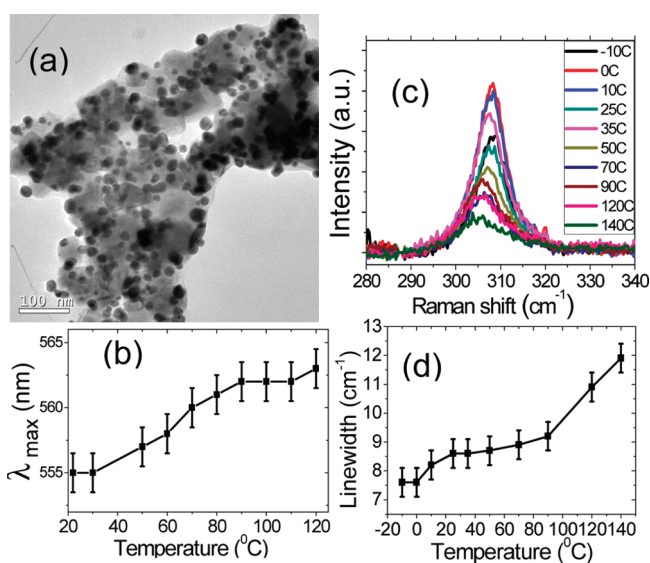

Figure 3. (a) TEM image of $\sim$10 nm GNPs attached to the 47 nm BTO NCs. **(b)** Temperature dependent plasmon peak wavelength of the GNPs shown in panel a. **(c)** Raman spectra around the 306 cm^{-1} band at different temperatures for the 47 nm BTO NCs. **(d)** Full width at half-maximum $\sim$306 cm^{-1} Raman peak as a function of temperature.

order of $\sim$1 nm (see Supporting Information Figures S4 and S5, respectively) which is roughly the experimental error limit, indicating that the LSPR shift shown in Figure 1b was due to the change in the dielectric constant of the BTO NPs. The intrinsic temperature dependence of the LSPR of small GNPs was studied by Doremus[59] and Link and El-Sayed[60] and found to be negligible within the range of temperatures used in this work.

Complementary temperature-dependent high resolution Raman spectroscopy experiments were also carried out on the same BTO NC samples (see Supporting Information Figure S6). A series of temperature-dependent Raman spectra of the 16 $\pm$ 4 nm BTO NPs is shown in Figure 2a. The spectrum is focused on the mixed E(LO + TO) and B$_1$(TO) soft mode at $\sim$306 cm^{-1} which appears to decrease in intensity and broaden sharply as the temperature increases through $\sim$30 °C. These spectral changes were previously used to characterize T_C in bulk BTO.[32] Figure 2b displays the change in the line width of the $\sim$306 cm^{-1} Raman peak with increasing temperature exhibiting a sharp transition at about $\sim$30 °C similar to the LSPR shifts displayed in Figure 1b. The line width continues to moderately increase and finally levels at about 90 °C. It is well established, that while ideally the Raman lines of BTO should completely disappear above T_C, they usually only decrease in magnitude and broaden, in particular in NCs, possibly due to an order−disorder transition component and local distortions related to the NC surfaces[61,62] which will be discussed later on.

Consequently, it appears that both the LSPR peak shift, through the electronic response of the BTO NCs, and the Raman peak intensity and line width, which directly probe structural changes in the BTO nanocrystals, were able to detect close transition temperatures in the range of $\sim$25−30 °C for the 16 $\pm$ 4 nm BTO NCs which is in agreement with early estimates on size-dependent T_C of BTO nanopowders.[16] The similarity between the temperature dependent LSPR data obtained on the BTO-GNP hybrids and the Raman data obtained on the pure BTO NCs indicates that the attached GNPs do not significantly affect the phase transition at the BTO NCs.

The LSPR peak position in the Au−BTO samples is in the range of 555−565 nm instead of the $\sim$525 nm for a solution of $\sim$10 nm isolated GNPs. This red-shift is due to both the higher dielectric constant of the BTO, relative to the solvent, and due to inter-GNP interactions occurring when the GNPs are densely adsorbed on the BTO NC surfaces, which cause LSPR peak red-shifting and broadening.[63]

The plasmon peak of the GNPs coating the relatively larger BTO NCs of 47 $\pm$ 11 nm shown in Figure 3a continuously shifts to the red with increasing temperature up to a temperature of $\sim$90 °C (Figure 3b). The line width of the 306 cm^{-1} Raman peak increases

gradually with temperature and undergoes a major change from about 90 °C and up.

BTO NCs of size >0.1 μm with presumably bulk-like properties were coated with GNPs as depicted in Figure 4a. The temperature-dependent λ_{max} of the GNPs coating the bulk-like BTO NCs plotted in Figure 4b moderately shifts to longer wavelengths until a sharp red-shift is clearly seen when the temperature reaches ~130 °C, in accordance with bulk T_C. The existence of a continuous shift in the temperature range of 50−90 °C, much lower than the jump occurring at 130 °C, can be explained by the BTO NC size distribution which is broad enough to contain smaller NCs of ~50 nm. The line width of the ~306 cm^{-1} Raman peak also displays a continuous increase as a function of temperature (Figure 4d) which levels above 120 °C. The relatively smaller steps starting at 20 °C and at 50 °C probably also originate in the size distribution of the BTO NCs in the bulk-like sample.

In general, it seems that the changes in the optical dielectric constant, which represents the electronic response, and the transitions in the nuclear configuration (Raman) with temperature follow closely. Both LSPR and Raman signal results on the 47 ± 11 nm and bulk-like BTO agree well with the previous reports on size-dependent T_C of BTO.[16,17,20]

The phase transition observed in both signals in the 16 ± 4 nm BTO NCs at *ca.* 25−30 °C is surprisingly sharp in contrast to the much more gradual transitions observed in the signals from two larger BTO NC samples. Assuming a size-dependent T_C model, and considering that the 16 ± 4 nm NCs are close to the proposed critical size, one would expect that the size, stoichiometry, and defect distributions for these NCs would cause a complete smearing of the phase transition as a function of temperature.[26] Hence, the observation of a sharp transition indicates against this model, and supports the notion of the domination of surface contribution to the transition at this size regime, which is not size dependent.[16] The influence of stoichiometry deviations on T_C, possibly occurring at the smaller NCs or at the surface of the larger NCs, is rather hard to probe[26] and may potentially affect the phase transition temperature of the NCs.

At the small size regime (16 ± 4 nm), where both probes sample the whole NC volume, they should both display a similar temperature dependence as indeed was observed. For the two larger BTO NC samples the situation is different, where the LSPR probe would only be sensitive to the surface of the NCs while the Raman probe still samples the whole NC volume.

To understand the results for the two larger NC samples we classify them as pertaining to two size regimes, categorically different from the small size regime. The two probes roughly show the same behavior for the bulk-like NC size regime, which exhibits a transition at the bulk T_C (120−130 °C), as expected from
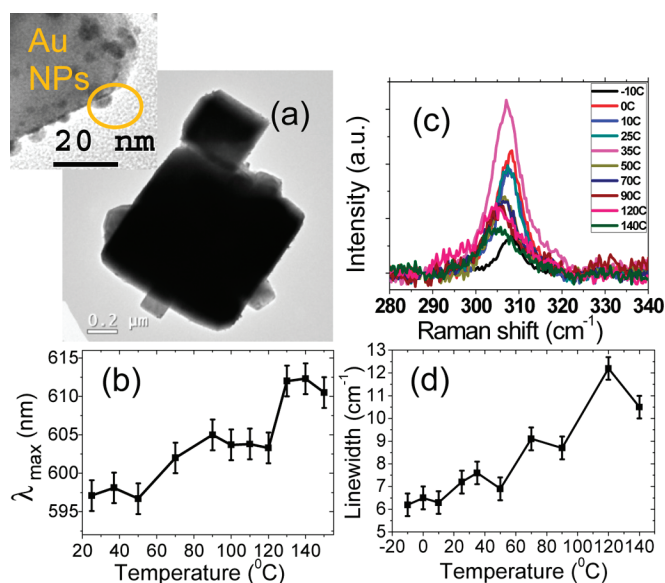

Figure 4. (a) TEM image of ~10 nm GNPs attached to the bulk-like BTO NCs. Inset shows the GNPs attached to the facet of a BTO crystal. (b) Temperature-dependent plasmon peak position of the GNPs shown in panel a. (c) Raman spectra around the 306 cm^{-1} band at different temperatures for the bulk BTO NCs. (d) Full width at half-maximum of the ~306 cm^{-1} Raman peak as a function of temperature.

>100 nm NCs, with additional transitions at lower temperatures, probably corresponding to smaller NCs from the intermediate size regime.

The intermediate size regime (47 ± 11 nm) is characterized by somewhat different temperature dependences of the LSPR and Raman probes. This is probably due to competing surface and interior, bulk-like behaviors of the ferroelectric-to-paraelectric transition. A possible explanation for the difference between the results of the two probes in the intermediate size regime is that the BTO NCs have interiors and surfaces that behave differently and undergo the ferroelectric-to-paraelectric transitions at different temperatures.

Interestingly, on cooling the samples after the heating cycle the LSPR measurements revealed a thermal hysteresis in the plasmon peak position of the GNPs attached to the BTO NCs. The hysteresis appeared in all the three 16 nm (Figure 5a), 47 nm (Figure 5b), and bulk-like BTO particle sample (Figure 5c), while for the Raman probe a small hysteresis only appeared for the small size regime (16 ± 4 nm BTO shown in Figure 5d) around 30−80 °C. This significant difference in hysteresis between the two techniques, in spite of the similarity in the observed changes in LSPR peak shift and Raman line width as a function of temperature, again indicates the fundamental difference between the two techniques. It should be stressed that also in this case the LSPR experiments with the control samples of GNPs only and GNPs attached to STO spread on a silica substrate or dispersed in tetraethylene glycol did not show any visible hysteresis.

Unlike the small hysteresis in the bulk-like BTO sample, the larger hysteresis in the small and interme-
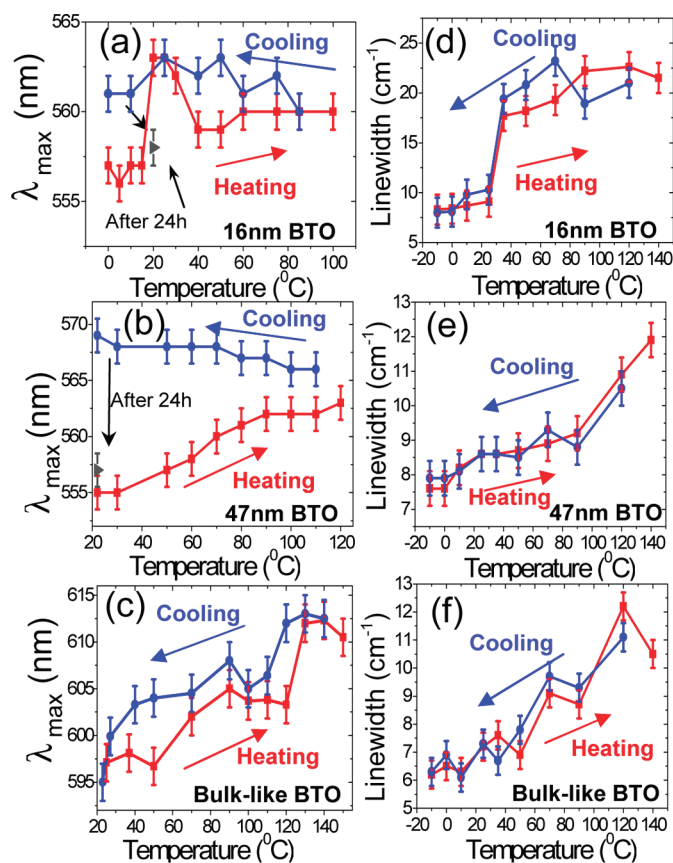
Figure 5. Thermal hysteresis in the BTO NCs. (a−c) Hysteresis in the LSPR peak shift on heating *vs* cooling of the GNPs attached to the 16 nm, 47 nm, and bulk-like BTO samples, respectively. The arrows indicate the measured λ_{max} at room temperature 24 h after cooling. (d−f) Linewidth of the 306 cm^{-1} Raman peak as function of temperature on heating *vs* cooling for the 16 nm, 47 nm, and bulk-like BTO samples, respectively.

diate size BTO NC samples did not disappear at low temperatures. The simpler explanation to this phenomenon is that the T_C for the bulk-like NCs is higher than the other two samples, and cooling to room temperature in this sample takes the system farther down from T_C, to return to the polar state. Furthermore, repeating the LSPR measurement 24 h after cooling in the smaller NC samples revealed that the plasmon peak returned to its original wavelength, depicted by the arrows in Figure 5 panels a and b.

The large hysteresis appearing at the smaller BTO NC samples (16 and 47 nm) when probed by the LSPR but absent from the Raman data reflects the unique sensitivity of the LSPR probe to the NC surfaces and indicates that the polarization at the surface of the NCs in the small and intermediate size regimes behaves differently than in their interior. The small hysteresis in the Raman signal for the small size regime shows that the whole NC transition is affected by the surface. On the other hand, the small hysteresis observed by the LSPR for the bulk-like sample indicates domination of the interior over the surface in this size regime.

It seems that while the transition temperatures of the near surface volume and the whole NC volume are

typically close, in particular at the small size regime, the ferroelectric relaxation processes could be very slow for the near-surface volume. Theoretical work by Morozovska and Eliseev demonstrated that the relaxation times among other correlation functions and related dynamical properties strongly depend on the surface energy and finite size effects, which increases with particle size decrease.[64] The polarization in ferroelectric surfaces is compensated by mobile charge carriers in the crystal and adsorption of molecules, such as water, on the crystal. Studies by Kalinin, Johnson, and Bonnell[41] of BTO single crystal (100) surfaces using scanning probe methods revealed that temperature- and time-dependent behavior of surface potential are governed by the rapid nuclear polarization dynamics (*i.e.* within the interior part of the ferroelectric) and slow screening charge dynamics (*i.e.* at the surface). The observed LSPR hysteresis on cooling from the paraelectric state of the BTO NCs originates from slow changes of the surface polarization which should be strongly temperature dependent. The LSPR shifts are due to optical dielectric constant changes that are dominated by the tightly bound electrons which respond to the changes in nuclear configurations.

The general observation of a residual Raman signal in BTO crystals above T_C has been attributed to remaining nanoscale polar regions.[65] This is also clearly observed in the BTO NC samples of the present work. An interesting difference can be noted between the small size NC sample and the larger samples, as reflected in the magnitude of the line broadening on crossing T_C. The sharp broadening of the Raman line of the 16 ± 4 nm sample is almost twice the maximal broadening observed for the other two samples. This roughly temperature-independent large broadening (and intensity, see Figure 2a) beyond T_C is probably purely a surface contributed signal which is induced by disordered polar-distortions.[62] In the larger NCs this surface contribution is probably small and the temperature-dependent broadening and intensity drop (Figures 3c and 4c) may be related to the above-mentioned ordered polar nanodomains within the interior of the NCs. These regions produce narrower Raman lines that disappear with increasing temperature above T_C.

CONCLUSION

A new technique to probe the temperature-dependent surface behavior of ferroelectric materials has been demonstrated, which together with a Raman spectroscopic probe provides an interesting picture on the size dependence of the ferroelectric-to-paraelectric phase transition in nanoscale ferroelectrics. In the smaller BTO NCs the surface (LSPR data) and volume (Raman data) correlate well due to dominance of the surface over the whole NC behavior. Also at the bulk-like NCs the surface and volume data agree, due to dominance of the volume over the whole NC behavior,

but at the intermediate sizes the surface and volume behave differently. The volume T_C is probably close to bulk-like in all but the smallest NCs where it decreases significantly relative to the bulk value. The surface ferroelectricity seems to behave differently from the volume ferroelectricity and is characterized by very long relaxation time scales. This behavior could be the result of a stoichiometry deviation and/or the intrinsic high defect concentration at the surface. This work strengthens the concept of having different surface and interior, bulk-like contributions to the ferroelectricity and to the phase transition and agrees well with a similar notion already discussed with respect to ferroelectric thin films.[14] It thus indicates the absence of an intrinsic size-dependence of the transition temperature. Owing to the high scattering cross-section of the gold coating the BTO NCs, this LSPR-based sensing technique could be extended toward probing single ferroelectric NCs coated with GNPs by combining high resolution optical microscopy with temperature dependent spectroscopy. Studying the ferroelectric phase transition on a single NC level may further enrich our knowledge on the nature of this elusive type of phase transition.

METHODS

Preparation of BaTiO$_3$ (BTO) Nanocrystals (NCs). BTO NCs preparation is based on a synthesis published by Liu *et al.*[58] The BTO NPs were prepared in a molten eutectic mixture at relatively low temperatures without using an organic dispersant or capping agent. Size selectivity was attained by changing the procedure temperature. Molten eutectic potassium hydroxide and sodium hydroxide mixtures at ~180 and ~230 °C yielded BTO NCs of 47 ± 11 and 200 ± 140 nm (commonly accepted as bulk-like) in size, respectively. A molten eutectic CsOH and RbOH mixture at ~120 °C yielded BTO NPs of 16 ± 4 nm in size. In a typical preparation, 20 g of mixed hydroxides (NaOH/KOH = 51.5/48.5) was placed in a 25 mL Teflon vial. A mixture of BaCl$_2$ salt and TiO$_2$ NPs (5−20 nm), 0.5 mmol each, was used as the raw material for reaction. The raw material was placed on the top of the hydroxide in the vial. The vial was put into a preheated oven at the appropriate temperature according to the required NC size. After the hydroxides melted, the vial was shaken to ensure uniformity of the mixed reactants. After reacting for 48 h (96 h for the bulk-like BTO sample) the vial was taken out and cooled to room temperature. Deionized (DI) water was added to the solid product. The product was filtered and washed with DI water.

Coating BTO NCs with GNPs. Two different approaches were implemented to coat the BTO NCs with ~10 nm Au nanoparticles (GNPs).

First Method, Used for Coating the Bulk-like BTO NCs with GNPs: GNPs were synthesized by reduction of 10 mL of HAuCl$_4$ 2.0 mM with 375 μL of NaBH$_4$ 0.11 M in the presence of thioctic acid (TA) as a surfactant (100:1 Au:TA) and tuning the pH to *ca.* 8−9 using 0.1 M KOH solution. The BTO and GNPs were mixed (1:2−5 BTO:Au volume ratio) for two days, allowing the two types of particles bind. Thereafter, the solution was centrifuged and redispersed in DI water twice to exclude GNPs that were not attached to BTO crystals. The solution was filtered and washed with DI water, finally receiving pure BTO NCs coated with GNPs.

The BTO NCs coated with GNPs were then deposited on a fused silica substrate by a modified layer by layer (LBL) method.[66] The silica was first cleaned in a piranha solution (H$_2$SO$_4$:H$_2$O$_2$ 3:1 volume ratio) for roughly 1 h. After washing with DI water and drying with N$_2$, the substrate was dipped into 1 wt % aminopropyltrimethoxy-silane (APTMS) in methanol for 2 h, acting as an anchor for GNPs to attach to the silica. Thereafter, the substrate was alternately dipped, 10 min to 1 h, in the BTO−GNPs dispersion and in poly-L-lyzine solution for 10−30 min each for about 5−10 cycles. The substrate was then washed with DI water between the dipping steps. In this way GNP aggregates that red-shift and broaden the plasmon peak were avoided, unlike the attempts of using drop casting or spin-coating methods to produce the films.

Second Method, for the 16 and 47 nm BTO NCs: A two-step preparation technique was implemented: first, gold seeds (1−2 nm) were prepared by reduction of HAuCl$_4$ with NaBH$_4$ in the presence of mercaptopropionic acid (MPA) as the surfactant. Coating the BTO NCs with these GNPs was performed as with the previously mentioned GNPs made with the TA surfactant. Second, the gold seeds on the BTO NCs were grown to ~10 nm GNPs by mixing them with a previously prepared solution containing 250 μL of HAuCl$_4$ 2.0 mM, 0.8 g of CTAB surfactant, and 212 μL of sodium ascorbate 0.33 mM in 8 mL of H$_2$O, while keeping the solution around 35 °C to avoid precipitation of CTAB. The advantage in this procedure is that the gold ions in the solution are reduced locally only on the previously prepared gold seeds that are already coating the BTO NPs. The gold-coated BTO NCs were then washed, filtered, and dispersed in tetraethyleneglycol, which has a relatively higher boiling temperature than water so temperature-dependent LSPR experiments were enabled directly on the solution. (Caution! piranha, APTMS, sodium borohydride, and chlorauric acid present potential health or fire hazards. Appropriate precautions should be observed at all times).

Coating SrTiO$_3$ (STO) NCs with Au NPs. STO NCs were purchased from Sigma Aldrich Co. The preparation of GNPs coated STO NCs and their characterization by LSPR is the same as for the bulk-like BTO NCs.

LSPR Measurements. Temperature dependent absorbance measurements were performed (1) on a Chirascan spectrometer (Applied Photophysics) equipped with temperature-controlled cell holder in a standard fused silica cell for the Au-coated BTO NCs in solution and (2) using a fiber-coupled array spectrometer (Ocean Optics, S2000) connected to a home-built temperature-controlled sample holder unit for the Au-coated BTO NCs deposited on the silica substrates. Spectra were taken at selected temperatures after stabilizing the temperature. The plasmon band peak position was estimated by fitting a Gaussian function.

Raman Spectroscopy. The Raman system comprised a Jobin-Yvon LabRam HR 800 micro-Raman system, equipped with a liquid-N$_2$-cooled detector. The excitation source was a He−Ne laser (633 nm) with a power of 5 mW on the sample. The laser was focused with an ×50 long-focal-length objective to a spot of about 2 μm. Measurements were taken with a 1800 grooves per mm grating and a confocal microscope with a 100 μm pinhole and a typical exposure time of 2 min. The temperature control unit is Linkam TMS 94 with a THMS600 stage spanning the range of −196 to 600 °C. A spectrum from a Si wafer was taken at every two to three temperatures in order to verify the stability of the Raman system. The line profiles were fitted with Lorentzian functions.

Transmission Electron Microscopy (TEM). TEM imaging was done on a Tecnai F20 (FEI).

Simulation of the GNP LSPR Peak Shift with Change in BTO Refractive Index on Reaching T_C. Finite difference time domain (FDTD) numerical solution of Maxwell's equations using the Lumerical software package (Lumerical Solutions, Inc.) was used to simulate the extinction spectrum of a 10 nm GNP attached to the center of a facet of a 20 nm BTO nanocube immersed in tetraethylene glycol. The RI values of BTO at room temperature and at bulk T_C were taken from ref 47.

REFERENCES AND NOTES

1. Scott, J. F. Applications of Modern Ferroelectrics. *Science* **2007**, *315*, 954–959.

2. Setter, N.; Damjanovic, D.; Eng, L.; Fox, G.; Gevorgian, S.; Hong, S.; Kingon, A.; Kohlstedt, H.; Park, N. Y.; Stephenson, G. B.; *et al.* Ferroelectric Thin Films: Review of Materials, Properties, and Applications. *J. Appl. Phys.* **2006**, *100*, 051606.

3. Shaw, T.; Trolier-McKinstry, S.; McIntyre, P. The Properties of Ferroelectric Films at Small Dimensions. *Annu. Rev. Mater. Sci.* **2000**, *30*, 263–298.

4. Gregg, J. M. Ferroelectrics at the Nanoscale. *Phys. Stat. Solidi A.* **2009**, *206*, 577–587.

5. Dawber, M.; Rabe, K.; Scott, J. Physics of Thin-Film Ferroelectric Oxides. *Rev. Mod. Phys.* **2005**, *77*, 1083.

6. Ahn, C. H.; Rabe, K. M.; Triscone, J. Ferroelectricity at the Nanoscale: Local Polarization in Oxide Thin Films and Heterostructures. *Science* **2004**, *303*, 488–91.

7. Rudiger, A.; Schneller, T.; Roelofs, A.; Tiedke, S.; Schmitz, T.; Waser, R. Nanosize Ferroelectric Oxides—Tracking Down the Superparaelectric Limit. *Appl. Phys. A: Mater. Sci. Process.* **2005**, *80*, 1247–1255.

8. Junquera, J.; Ghosez, P. Critical Thickness for Ferroelectricity in Perovskite Ultrathin Films. *Nature.* **2003**, *422*, 506–9.

9. Akdogan, E. K.; Safari, A. Thermodynamic Theory of Intrinsic Finite-Size Effects in PbTiO$_3$ Nanocrystals. I. Nanoparticle Size-Dependent Tetragonal Phase Stability. *J. Appl. Phys.* **2007**, *101*, 064114.

10. Ponomareva, I.; Naumov, I.; Kornev, I.; Fu, H.; Bellaiche, L. Modelling of Nanoscale Ferroelectrics from Atomistic Simulations. *Curr. Opin. Solid State Mater. Sci.* **2005**, *9*, 114–121.

11. Meyer, B.; Vanderbilt, D. *Ab Initio* Study of BaTiO$_3$ and PbTiO$_3$ Surfaces in External Electric Fields. *Phys. Rev. B.* **2001**, *63*, 205426.

12. Lichtensteiger, C.; Dawber, M.; Triscone, J. Ferroelectric Size Effects. In *Physics of Ferroelectrics*; Topics in Applied Physics; Springer Berlin/Heidelberg, 2007; Vol. 105, pp 305–338, and references therein 91–114.

13. Smith, M. B.; Page, K.; Siegrist, T.; Redmond, P. L.; Walter, E. C.; Seshadri, R.; Brus, L. E.; Steigerwald, M. L. Crystal Structure and the Paraelectric-to-Ferroelectric Phase Transition of Nanoscale BaTiO$_3$. *J. Am. Chem. Soc.* **2008**, *130*, 6955–63.

14. Bune, A. V.; Fridkin, V. M.; Ducharme, S.; Blinov, L. M.; Palto, S. P.; Sorokin, A. V.; Yudin, S. G.; Zlatkin, A. Two-Dimensional Ferroelectric Films. *Nature* **1998**, *391*, 874–877.

15. Chang, L. W.; McMillen, M.; Morrison, F. D.; Scott, J. F.; Gregg, J. M. Size Effects on Thin Film Ferroelectrics: Experiments on Isolated Single Crystal Sheets. *Appl. Phys. Lett.* **2008**, *93*, 132904.

16. Tanaka, M.; Makino, Y. Finite Size Effects in Submicron Barium Titanate Particles. *Ferroelectrics Lett. Sec.* **1998**, *24*, 13–23.

17. Hoshina, T.; Kakemoto, H.; Tsurumi, T.; Wada, S.; Yashima, M. Size and Temperature-Induced Phase Transition Behaviors of Barium Titanate Nanoparticles. *J. Appl. Phys.* **2006**, *99*, 054311.

18. Zhong, W. L.; Jiang, B.; Zhang, P. L.; Ma, J. M.; Cheng, H. M.; Yang, Z. H. Phase Transition in PbTiO$_3$ Ultrafine Particles of Different Sizes. *J. Phys.: Condens. Matter.* **1993**, *5*, 2619–2624.

19. Frey, M.; Payne, D. Grain-Size Effect on Structure and Phase Transformations for Barium Titanate. *Phys. Rev. B.* **1996**, *54*, 3158–3168.

20. Spanier, J. E.; Kolpak, A. M.; Urban, J. J.; Grinberg, I.; Ouyang, L.; Yun, W. S.; Rappe, A. M.; Park, H. Ferroelectric Phase Transition in Individual Single-Crystalline BaTiO$_3$ Nanowires. *Nano Lett.* **2006**, *6*, 735–739.

21. Fong, D. D.; Stephenson, G. B.; Streiffer, S. K.; Eastman, J. A.; Auciello, O.; Fuoss, P. H.; Thompson, C. Ferroelectricity in Ultrathin Perovskite Films. *Science* **2004**, *304*, 1650–3.

22. Tybell, T.; Ahn, C. H.; Triscone, J.-M. Ferroelectricity in Thin Perovskite Films. *Appl. Phys. Lett.* **1999**, *75*, 856.

23. Drezner, Y.; Berger, S. Nanoferroelectric Domains in Ultrathin BaTiO$_3$ Films. *J. Appl. Phys.* **2003**, *94*, 6774.

24. Prosandeev, S.; Ponomareva, I.; Naumov, I.; Kornev, I.; Bellaiche, L. Original Properties of Dipole Vortices in Zero-Dimensional Ferroelectrics. *J. Phys.: Condens. Matter.* **2008**, *20*, 193201.

25. Petkov, V.; Buscaglia, V.; Buscaglia, M. T.; Zhao, Z.; Ren, Y. Structural Coherence and Ferroelectricity Decay in Submicron- and Nano-Sized Perovskites. *Phys. Rev. B.* **2008**, *78*, 1–7.

26. Lee, S.; Rossetti, G. A.; Liu, Z.; Randall, C. A. Influence of Nonstoichiometry on Ferroelectric Phase Transition in BaTiO$_3$. *J. Appl. Phys.* **2009**, *105*, 093519.

27. Choi, K. J.; Biegalski, M.; Li, Y. L.; Sharan, A.; Schubert, J.; Uecker, R.; Reiche, P.; Chen, Y. B.; Pan, X. Q.; Gopalan, V.; *et al.* Enhancement of Ferroelectricity in Strained BaTiO$_3$ Thin Films. *Science* **2004**, *306*, 1005–9.

28. Nonnenmann, S.; Spanier, J. Ferroelectricity in Chemical Nanostructures: Proximal Probe Characterization and the Surface Chemical Environment. *J. Mater. Sci.* **2009**, *44*, 5205–5213.

29. Bratkovsky, A.; Levanyuk, A. Smearing of Phase Transition Due to a Surface Effect or a Bulk Inhomogeneity in Ferroelectric Nanostructures. *Phys. Rev. Lett.* **2005**, *94*, 1–4.

30. Bin-Omran, S.; Kornev, I.; Ponomareva, I.; Bellaiche, L. Diffuse Phase Transitions in Ferroelectric Ultrathin Films from First Principles. *Phys. Rev. B.* **2010**, *81*, 094119.

31. Hoshina, T.; Wada, S.; Kuroiwa, Y.; Tsurumi, T. Composite Structure and Size Effect of Barium Titanate Nanoparticles. *Appl. Phys. Lett.* **2008**, *93*, 192914.

32. Tenne, D. a.; Xi, X. Raman Spectroscopy of Ferroelectric Thin Films and Superlattices. *J. Am. Ceram. Soc.* **2008**, *91*, 1820–1834, and therein references 25–34.

33. Li, S.; Eastman, J. A.; Li, Z.; C.M, F.; Newnham, R.; Cross, L. E. Size Effects in Nanostructured Ferroelectrics. *Phys. Lett. A.* **1996**, *212*, 341–346.

34. Kretschmer, R.; Binder, K. Surface Effects on Phase Transitions in Ferroelectrics and Dipolar Magnets. *Phys. Rev. B.* **1979**, *20*, 1065–1076.

35. Gruverman, A.; Kholkin, A. Nanoscale Ferroelectrics: Processing, Characterization and Future Trends. *Rep. Prog. Phys.* **2006**, *69*, 2443–2474.

36. Bonnell, D. A.; Kalinin, S. V.; Kholkin, A. L.; Gruverman, A. Piezoresponse Force Microscopy: A Window into Electromechanical Behavior at the Nanoscale. *MRS Bull.* **2009**, *34*, 648–657.

37. Kalinin, S. V.; Rodriguez, B. J.; Jesse, S.; Karapetian, E.; Eliseev, E. A.; Mirman, B.; Morozovska, A. N. Nanoscale Electromechanics of Ferroelectric and Biological Systems: A New Dimension in Scanning Probe Microscopy. *Annu. Rev. Mater. Res.* **2007**, *37*, 189–238.

38. Eng, L. M.; Güntherodt, H.; Schneider, G. a.; Köpke, U.; Muñoz, Saldaña. J. Nanoscale Reconstruction of Surface Crystallography from Three-Dimensional Polarization Distribution in Ferroelectric Barium–Titanate Ceramics. *Appl. Phys. Lett.* **1999**, *74*, 233.

39. Tybell, T.; Paruch, P.; Giamarchi, T.; Triscone, J. Domain Wall Creep in Epitaxial Ferroelectric Pb(Zr$_{0.2}$Ti$_{0.8}$)O$_3$ Thin Films. *Phys. Rev. Lett.* **2002**, *89*, 8–11.

40. Hidaka, T.; Maruyama, T.; Saitoh, M.; Mikoshiba, N.; Shimizu, M.; Shiosaki, T.; Wills, L. A.; Hiskes, R.; Dicarolis, S. A.; Amano, J.; *et al.* Formation and Observation of 50 nm Polarized Domains in PbZr$_{1-x}$Ti$_x$O$_3$ Thin Film Using

Scanning Probe Microscope. *Appl. Phys. Lett.* **1996**, *68*, 2358.

41. Kalinin, S. V.; Johnson, C. Y.; Bonnell, D. A. Domain Polarity and Temperature Induced Potential Inversion on the BaTiO$_3$(100) Surface. *J. Appl. Phys.* **2002**, *91*, 3816.

42. Mulvaney, P. Surface Plasmon Spectroscopy of Nanosized Metal Particles. *Langmuir* **1996**, *12*, 788–800.

43. Willets, K. A.; Van Duyne, R. P. Localized Surface Plasmon Resonance Spectroscopy and Sensing. *Annu. Rev. Phys. Chem.* **2007**, *58*, 267–297.

44. Jain, P. K.; Huang, X.; El-Sayed, I. H.; El-Sayed, M. A. Noble Metals on the Nanoscale: Optical and Photothermal Properties and Some Applications in Imaging, Sensing, Biology, and Medicine. *Acc. Chem. Res.* **2008**, *41*, 1578–1586.

45. Oldenburg, S.; Averitt, R. D.; Westcott, S. L.; Halas, N. J. Nanoengineering of Optical Resonances. *Chem. Phys. Lett.* **1998**, *288*, 243–247.

46. Kelly, K. L.; Coronado, E.; Zhao, L. L.; Schatz, G. C. The Optical Properties of Metal Nanoparticles: The Influence of Size, Shape, and Dielectric Environment. *J. Phys. Chem. B* **2003**, *107*, 668–677.

47. Miller, M. M.; Lazarides, A. A. Sensitivity of Metal Nanoparticle Surface Plasmon Resonance to the Dielectric Environment. *J. Phys. Chem. B* **2005**, *109*, 21556–21565.

48. Mock, J. J.; Smith, D. R.; Schultz, S. Local Refractive Index Dependence of Plasmon Resonance Spectra from Individual Nanoparticles. *Nano Lett.* **2003**, *3*, 485–491.

49. Underwood, S.; Mulvaney, P. Effect of the Solution Refractive Index on the Color of Gold Colloids. *Langmuir* **1994**, *10*, 3427–3430.

50. Larsson, E. M.; Langhammer, C.; Zorić, I.; Kasemo, B. Nanoplasmonic Probes of Catalytic Reactions. *Science* **2009**, *326*, 1091–1094.

51. Stuart, D. A.; Haes, A. J.; Yonzon, C. R.; Hicks, E. M.; Van Duyne, R. P. Biological Applications of Localised Surface Plasmonic Phenomenae. *IEEE Proc. Nanobiotechnol.* **2005**, *152*, 13–32.

52. Lal, S.; Clare, S. E.; Halas, N. J. Nanoshell-Enabled Photothermal Cancer Therapy: Impending Clinical Impact. *Acc. Chem. Res.* **2008**, *41*, 1842–1851.

53. Lal, S.; Grady, N. K.; Kundu, J.; Levin, C. S.; Lassiter, J. B.; Halas, N. J. Tailoring Plasmonic Substrates for Surface Enhanced Spectroscopies. *Chem. Soc. Rev.* **2008**, *37*, 898–911.

54. Veithen, M.; Ghosez, P. Temperature Dependence of the Electro-optic Tensor and Refractive Indices of BaTiO$_3$ from First Principles. *Phys. Rev. B* **2005**, *71*, 132101.

55. Merz, W. The Electric and Optical Behavior of BaTiO$_3$ Single-Domain Crystals. *Phys. Rev.* **1949**, *76*, 1221–1225.

56. Ringe, E.; McMahon, J. M.; Sohn, K.; Cobley, C.; Xia, Y.; Huang, J.; Schatz, G. C.; Marks, L. D.; Van Duyne, R. P. Unraveling the Effects of Size, Composition, and Substrate on the Localized Surface Plasmon Resonance Frequencies of Gold and Silver Nanocubes: A Systematic Single-Particle Approach. *J. Phys. Chem. C* **2010**, *114*, 12511–12516.

57. Duval Malinsky, M.; Kelly, K. L.; Schatz, G. C.; Van Duyne, R. P. Nanosphere Lithography: Effect of Substrate on the Localized Surface Plasmon Resonance Spectrum of Silver Nanoparticles. *J. Phys. Chem. B* **2001**, *105*, 2343–2350.

58. Liu, H.; Hu, C.; Wang, Z. L. Composite-Hydroxide-Mediated Approach for the Synthesis of Nanostructures of Complex Functional-Oxides. *Nano Lett.* **2006**, *6*, 1535–1540.

59. Doremus, R. H. Optical Properties of Small Gold Particles. *J. Chem. Phys.* **1964**, *40*, 2389.

60. Link, S.; El-Sayed, M. A. Size and Temperature Dependence of the Plasmon Absorption of Colloidal Gold Nanoparticles. *J. Phys. Chem. B* **1999**, *103*, 4212–4217.

61. Stern, E. Character of Order−Disorder and Displacive Components in Barium Titanate. *Phys. Rev. Lett.* **2004**, *93*, 037601.

62. Page, K.; Proffen, T.; Niederberger, M.; Seshadri, R. Probing Local Dipoles and Ligand Structure in BaTiO$_3$ Nanoparticles. *Chem. Mater.* **2010**, *22*, 4386–4391.

63. Wang, H.; Levin, C. S.; Halas, N. J. Nanosphere Arrays with Controlled Sub-10-nm Gaps as Surface-Enhanced Raman Spectroscopy Substrates. *J. Am. Chem. Soc.* **2005**, *127*, 14992–14993.

64. Morozovska, A. N.; Eliseev, E. A. Surface and Finite Size Effect on Fluctuations Dynamics in Nanoparticles with Long-Range Order. *J. Appl. Phys.* **2010**, *107*, 044101.

65. Ziębińska, a.; Rytz, D.; Szot, K.; Górny, M.; Roleder, K. Birefringence above T_C in Single Crystals of Barium Titanate. *J. Phys.: Condens. Matter* **2008**, *20*, 142202.

66. Russell, L. E.; Galyean, A. A.; Notte, S. M.; Leopold, M. C. Stable Aqueous Nanoparticle Film Assemblies with Covalent and Charged Polymer Linking Networks. *Langmuir* **2007**, *23*, 7466–7471.